RSC Advances

PAPER

View Article Online
View Journal | View Issue

Cite this: *RSC Adv.*, 2021, **11**, 39625

Adjusting the photovoltaic performance of big fused ring-based small molecules by tailoring with different modifications†

Min Li, *[ab] Manjun Xiao*[c] and Zuojia Li*[a]

Received 10th November 2021
Accepted 1st December 2021

DOI: 10.1039/d1ra08239f

rsc.li/rsc-advances

Three novel A–D–A type small-molecule donor materials, namely **AAN-DPP$_2$**, **AAN(T-DPP)$_2$** and **AANT(T-DPP)$_2$**, with anthanthrene (**AAN**) as the electron-donating core, diketopyrrolopyrrole (DPP) as the electron-accepting moiety, and thiophene as π-bridge units, have been designed and synthesized for application in bulk-heterojunction (BHJ) organic solar cells (OSCs). Compared to **AAN-DPP$_2$**, devices based on **AAN(T-DPP)$_2$** and **AANT(T-DPP)$_2$** show better photovoltaic performance due to broader absorption and better planarity of the molecular backbone. A maximum power conversion efficiency (PCE) of 2.33% with a short-circuit current density (J_{sc}) of 6.82 mA cm^{-2} and a fill factor (FF) of 39.80 was obtained in the **AAN(T-DPP)$_2$**/PC$_{71}$BM-based solar cells. This is resulting from the suitable thickness of the active layer, improving the ability of catching light and decreasing the twist angle of the backbone by inserting a thiophene spacer. The results indicate that strategic substitution of π-bridges and side-chains in A–D–A type SMs is an efficient strategy to improve photovoltaic performance.

1. Introduction

Solution-processed organic solar cells (OSCs) are drawing more and more attention recently for their promising applications in next generation clean and renewable energy sources with the advantages of low cost, light weight, and high mechanical flexibility.[1–4] With the rapid progress over recent years, the best power conversion efficiency (PCE) of polymer donors in the single-junction and tandem solar cells has reached 18.22% and 17.3%, respectively.[5–8] Fortunately, the small molecular ternary and tandem OSCs have also achieved 13.6% and 12.7% PCEs, respectively,[9,10] and for the single-junction device field, a PCE of 11.5% has been achieved for solution-processed small molecule solar cells (SMSCs).[11] Furthermore, compared to polymers, small-molecules possess unique features of easy purification and well-defined discrete structure, which can ensure greater reproducibility in the device performance.[12] As being comparable with polymer materials, SM-OSCs have been considered being promising candidates for high efficient OPVs.

Notably, besides the high efficiency, "low cost" of OSCs also play as an important role in the commercialization process that should not be ignored. As we all known, a large amount of SMSCs with an A–D–A framework were synthesized and systematically investigated containing different donor cores such as dithienosilole (DTS), benzodithiophene (BDT), porphyrin.[13] Those molecules exhibit high mobilities and wide absorptions with high coefficients owing to the efficient conjugation in the backbone structure and intra-molecule charge transfer (ICT) between the terminal acceptor units and the central donor building blocks.[12] However, those classical donor cores are always hard to synthesize, in order to lower the cost, some cheap industrialized dyes may be taken into consideration.

In recent years, industrialized dyes have received attention in their potential as building blocks for organic semiconductors. Plenty of dyes possess a rigid and polycyclic π-conjugated framework, which contribute to making their optical spectra locate in the visible range. Besides the advantage of low price, they also often have modified positions that allow various functional groups to adjust their electronic and optical properties. The star industrialized dye that has been applied in organic semiconductors is diketopyrrolopyrrole (DPP).[14–16] Furthermore, DPP is also a success example for using as the electron acceptor unit in the organic solar cells (OSCs).[17] DPP dyes possess several advantages as follows: firstly, most of the DPP dyes show strong absorption with high molar extinction coefficients (ε_{max}) values; secondly, the highly ordered

[a]*Jiangxi Province Key Laboratory of Polymer Micro/Nano Manufacturing and Devices, School of Chemistry, Biology and Materials Science, East China University of Technology, Nanchang 330013, P. R. China. E-mail: lzjshihaoren@126.com*

[b]*School of Materials Science and Engineering, Jiangsu Engineering Laboratory of Light-Electricity-Heat Energy-Converting Materials and Applications, Jiangsu Collaborative Innovation Center of Photovoltaic Science and Engineering, National Experimental Demonstration Center for Materials Science and Engineering, Changzhou University, Changzhou 213164, China. E-mail: limin20a@126.com*

[c]*College of Chemistry, Key Lab of Environment-Friendly Chemistry and Application in the Ministry of Education, Xiangtan University, Xiangtan 411105, China. E-mail: xmj0704@163.com*

† Electronic supplementary information (ESI) available. See DOI: 10.1039/d1ra08239f

molecular stacking in the solid state endow DPP dyes with high hole and electron mobilities; thirdly, benefiting from the bicyclic lactam rings, DPP dyes show strong electron-withdrawing ability, which is suitable for using as an electron-deficient building block in donor–acceptor (D–A) synthetic strategy; finally, DPP-based conjugated molecules often exhibit a broad optical absorption and good film-forming characteristics as well as film morphology, resulting in high short-circuit current (J_{sc}) and good fill factor (FF) in solar cells.[18–20]

Prompted by this, we decided to investigate the photovoltaic properties of another industrialized dye called 4,10-dibromanthranthrone (ANT), or VAT Orange 3, the structure of which is depicted in Scheme 1. ANT has several obvious advantages: firstly, the bromine atoms at the 4- and 10-positions provide the opportunities to couple with other conjugated units, which can increase the effective conjugation length; secondly, the ketone group at 6- and 12-positions allows the introduction of alkyl chains to increase the solubility; thirdly, the symmetrical structure is likely to crystallize easily; finally, their extended π-conjugation, both in length and "area", which is beneficial for charge transport. Besides, their reorganization energies should be kept low because of their intrinsic structural rigidity. As we know, there are few reports in which anthanthrone is used as the starting material to prepare organic photovoltaic materials.[21–25]

In this work, we try to use ANT as the start material to build new donor core for OSCs. A series of A–D–A type small molecules was designed and synthesized, namely **AAN-DPP$_2$**, **AAN(T-DPP)$_2$** and **AANT(T-DPP)$_2$**, respectively (as shown in Chart 1), thiophene-flanked diketopyrrolopyrrole (TDPP) units used as the acceptor units, thiophene used as conjugated π-bridge, had been synthesized and characterized. Compared to **AAN-DPP$_2$**, **AAN(T-DPP)$_2$** and **AANT(T-DPP)$_2$** were appended with two thiophenes (T) as conjugated π-bridge. Accordingly, inserting extra thiophene unit into the space of the donor core and acceptor units have some advantages as below: firstly, increases effective conjugation of the molecular backbone, which translated into broader and stronger absorption result in higher short-circuit current density (J_{sc}); secondly, improve molecular planarity and enhance π-electron delocalization and solid-state intermolecular packing, which translated into higher hole mobility.[26–30] Though employing the electron-pushing thiophene π-bridge to the SMs may result in a little elevation to the HOMO energy level of donors often results in the decreasing of V_{oc} values,[31] while sometime can get a relatively higher J_{sc} value by sacrifice a little V_{oc}, and obtain a relatively higher PCE value at last. And in order to improve the solubility of the donor core, side-chains of 2-ethylheoxy and 2-octylthiophene were introduced into the **AAN** unit. Moreover, the introduction of side modified groups of 2-octylthiophene (T) to **AANT(T-DPP)$_2$** was expected to enhance the planarity of the whole molecule, and improve the fill factor (FF) values as well as make contribute to obtaining a higher current density (J_{sc}) by extend the conjugation. All these features are expected to improve the performance of SMSCs.[31–36]

The synthetic routes of **AAN-DPP$_2$**, **AAN(T-DPP)$_2$** and **AANT(T-DPP)$_2$** are shown in Scheme 1. By introducing thiophene units as π-bridge and side modified groups into the backbone of the SMs, their corresponding thermal, absorptive, electro-chemical and photovoltaic properties were rationally adjusted for applications as donor materials in OSCs. As results, all these SMs exhibit broad absorption spectra from the visible to near-infrared region. Due to the strong electron-withdrawing property of DPP fragment and relatively good planar backbone structure of three SMs, **AAN(T-DPP)$_2$** showed a narrower optical band gap of 1.72 eV. Under optimization, a maximum PCE of 2.33% along with J_{sc} of 6.82 mA cm^2, V_{oc} of 0.86 V, and FF of 39.80% was obtained in the **AAN(T-DPP)$_2$**/$PC_{71}BM$ based cells, which is about 1.22 and 1.15 times higher than that of **AAN-DPP$_2$**/$PC_{71}BM$ and **AANT(T-DPP)$_2$**/$PC_{71}BM$ based devices, respectively. Therefore, strategically substitution of π-bridge and side modified groups into the backbone of the SMs could be a promising strategy for adjusting the photovoltaic performance of **AAN**-based huge fused ring core molecular donor materials.

2. Experimental section

2.1. Materials and synthesis

All reactions were made under nitrogen atmosphere. All reagents and solvents were purchased from Acros and TCI Chemicals Inc., which were utilized unless stated otherwise. Toluene and tetrahydrofuran were dried and distilled according to common methods. **AAN** was synthesized according to the reported literature.[37] **DPP-Br** and **DPP-Bpi** were synthesized according to the reported literature.[38,39] The detailed syntheses of monomers were presented following the procedures described herein. The synthetic route is shown in Scheme 1 and their structures are consistent with molecular formulas characterized by ^{1}H NMR and MALDI-TOF in the Experimental section (Fig. S1–S19, see ESI†).

4,10-Dibromo-6,12-bis(octyloxy)anthanthrene (AAN). A three-neck round-bottom flask was charged with **ANT** (1 g, 2.16 mmol), aqueous NaOH (0.1 M, 100 mL, 10 mmol), Aliquat 336 (1060 mg, 1.2 mL, 2.62 mmol), $Na_2S_2O_4$ (970 mg, 5.56 mmol), and 2-ethylhexyl bromide (3 mL, 3.32 g, 17.24 mmol) under nitrogen atmosphere. The mixture was degassed for three times and heated at 80 °C for 3 h until the mixture turned colorless. The water was decanted and MeOH (60 mL) was added. The crude product was filtered and washed with MeOH. The crude product was purified by column chromatography (silica gel; eluent: petroleum ether : dichloromethane = 2 : 1) to afford **AAN** as an orange solid (1.09 g, 73%). ^{1}H NMR (400 MHz, $CDCl_3$, δ): 8.76 (d, J = 10.2 Hz, 4H), 8.62 (d, J = 7.5 Hz, 2H), 8.20 (t, J = 7.8 Hz, 2H), 4.21 (d, J = 5.4 Hz, 4H), 2.17–2.04 (m, 2H), 1.95–1.70 (m, 10H), 1.26 (s, 8H), 1.16 (t, J = 7.4 Hz, 6H), 1.03 (t, J = 6.3 Hz, 6H). ^{13}C NMR (100 MHz, $CDCl_3$, δ): 149.00, 129.11, 126.78, 126.54, 125.17, 125.05, 124.97, 123.96, 122.69, 122.01, 121.04, 120.50, 41.17, 30.48, 29.35, 23.96, 23.27, 14.29, 11.49.

4,10-Bis(2-thienyl)-6,12-bis(octyloxy)anthanthrene (AAN-T). A dry flask was charged with **AAN** (102 mg, 0.15 mmol), 2-tributylstannylthiophene (165 mg, 0.14 mL, 0.44 mmol), [$PdCl_2$(-PPh_3)$_2$] (5 mg, 0.007 mmol), and anhydrous toluene (7 mL) under nitrogen. The mixture was degassed three times and heated at 110 °C overnight. Once cooled, the mixture was

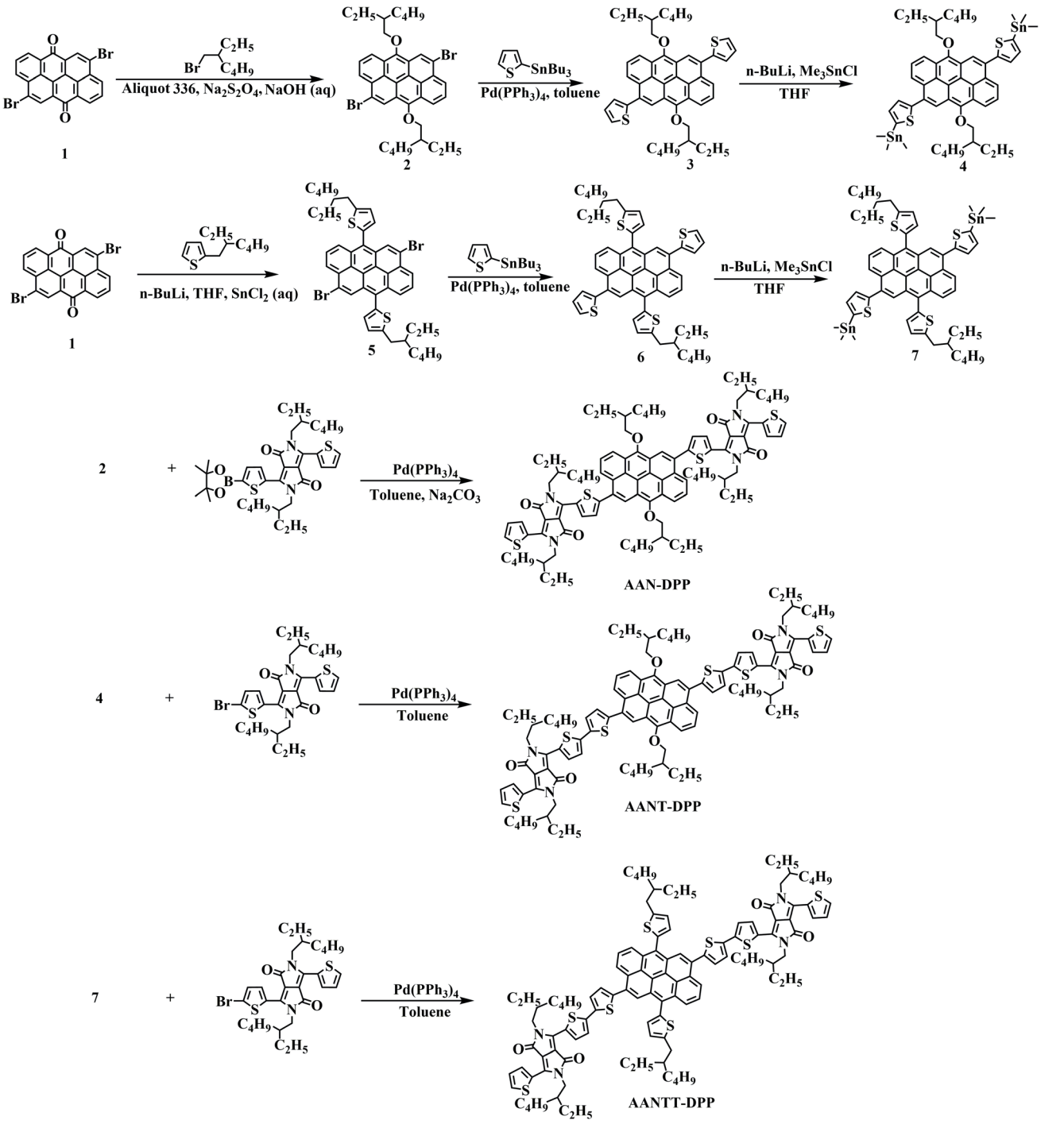

Scheme 1 Synthetic routes of SMs.

poured into MeOH. The precipitate was collected by filtration to afford **AAN-T** as an orange solid (87 mg, 85%). ^{1}H NMR (400 MHz, $CDCl_3$, δ): 8.84 (d, J = 8.0 Hz, 2H), 8.70–8.50 (m, 4H), 8.17 (t, J = 7.8 Hz, 2H), 7.55 (s, 4H), 7.32 (s, 2H), 4.29 (d, J = 5.3 Hz, 4H), 2.13 (s, 2H), 1.80 (dd, J = 44.0, 37.0 Hz, 8H), 1.25 (s, 8H), 1.12 (t, J = 7.1 Hz, 6H), 0.94 (d, J = 6.4 Hz, 6H). ^{13}C NMR (101 MHz, $CDCl_3$, δ): 149.95, 142.26, 132.24, 131.08, 127.55, 125.92, 125.53, 124.70, 124.19, 123.05, 121.41, 120.84, 119.70, 79.12, 41.27, 30.61, 29.42, 24.05, 23.26, 14.25, 11.55.

4,10-Bis(2-thienyl)-6,12-bis(octyloxy)anthanthrene (AAN-T-Sn). In a three-neck round-bottom flask, to a solution of **AAN-T** (0.174 g, 0.25 mmol) in anhydrous THF (30 mL) was added a solution of *n*-BuLi in hexane (0.33 mL, 1.6 M) dropwise under nitrogen atmosphere at −78 °C. The mixture was stirred at −78 °C for 2 h, then Me_3SnCl (0.525 mL, 1 M) was added. The reaction mixture was warmed up to room temperature (RT) and stirred for 12 h. The reaction was quenched with H_2O, and extracted with chloroform (CF) (25 mL × 3). The organic

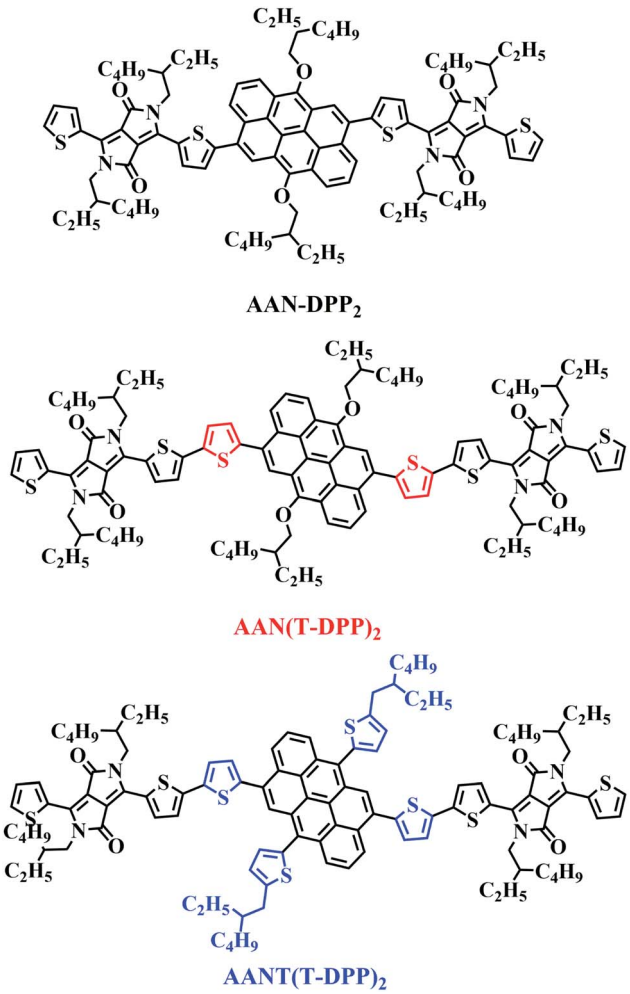

Chart 1 Chemical structures of SMs.

extracts were washed with brine and dried over anhydrous $MgSO_4$. After removal of the solvents under the reduced pressure, the **AAN-T-Sn** (250 mg, 98%) was obtained as an orange solid, and used in the next step without any further purification. ^{1}H NMR (400 MHz, $CDCl_3$, δ): 8.83 (d, J = 8.1 Hz, 2H), 8.66 (d, J = 7.5 Hz, 2H), 8.61 (s, 2H), 8.16 (t, J = 7.8 Hz, 2H), 7.68 (s, 2H), 7.39 (s, 2H), 4.29 (d, J = 5.3 Hz, 4H), 2.13 (dd, J = 11.5, 5.8 Hz, 2H), 2.00–1.62 (m, 8H), 1.51–1.31 (m, 8H), 1.13 (t, J = 7.3 Hz, 6H), 0.95 (t, J = 6.9 Hz, 6H), 0.67–0.23 (m, 18H). Anal. calcd for: $C_{52}H_{64}O_2S_2Sn_2$: C, 61.08; H, 6.31; S, 6.27. Found: C, 60.79; H, 6.40; S, 6.34.

4,10-Dibromo-6,12-bis(5-octyl-2-thienyl) anthanthrene (AANT). At 0 °C, a dry flask was charged with 2-octylthiophene (113 mg, 0.58 mmol) and anhydrous THF (3 mL) under nitrogen. A solution of *n*-BuLi in hexanes (2.5 M, 0.23 mL, 0.58 mmol) was added dropwise over 5 min. After 20 min at this temperature, this solution was transferred *via* cannula to a flask containing **ANT** (100 mg, 0.14 mmol) and anhydrous THF (10 mL) at 0 °C. After 1 h, a solution of tin(II) chloride dihydrate (400 mg, 1.78 mmol) in aqueous HCl (10% v/v, 4 mL) was added dropwise, and the resulting mixture was allowed to warm to RT over 1 h. Water was added to the reaction mixture, and the organic layer was extracted twice with CH_2Cl_2. The organic layer was dried with $MgSO_4$, and the solvent was evaporated under reduced pressure. The crude product was purified by silica gel column chromatography (CH_2Cl_2/hexanes = 1 : 2 v/v) followed by recrystallization in hexanes (at *ca.* −15 °C) to afford **AANT** as a yellow solid (57 mg, 39%). ^{1}H NMR (400 MHz, $CDCl_3$, δ): 8.83 (d, J = 8.1 Hz, 2H), 8.66 (d, J = 7.5 Hz, 2H), 8.61 (s, 2H), 8.16 (t, J = 7.8 Hz, 2H), 7.68 (s, 2H), 7.39 (s, 2H), 4.29 (d, J = 5.3 Hz, 4H), 2.13 (dd, J = 11.5, 5.8 Hz, 2H), 2.00–1.62 (m, 8H), 1.39 (dd, J = 44.9, 37.8 Hz, 12H), 1.13 (t, J = 7.3 Hz, 6H), 0.95 (t, J = 6.9 Hz, 6H), 0.67–0.23 (m, 12H). ^{13}C NMR (101 MHz, DMSO, δ): 146.86, 135.55, 131.31, 130.37, 130.03, 129.45, 128.42, 126.97, 126.53, 125.44, 124.53, 123.16, 121.44, 41.63, 34.45, 32.61, 29.02, 27.93, 26.91, 25.99, 23.13, 17.55, 14.29, 13.70, 11.09.

4,10-Bis(2-thienyl)-6,12-bis(5-octyl-2-thienyl) anthanthrene (AANT-T). A dry flask under argon was charged with **AANT** (102 mg, 0.15 mmol), 2-tributylstannylthiophene (165 mg, 0.14 mL, 0.44 mmol), [$PdCl_2(PPh_3)_2$] (5 mg, 0.007 mmol), and anhydrous toluene (7 mL). The mixture was degassed with a flow of argon for 10 min and heated at 80 °C overnight. Once cooled, the mixture was poured in MeOH. The precipitate was collected by filtration to afford **AANT-T** as an orange solid (87 mg, 85%). ^{1}H NMR (400 MHz, $CDCl_3$, δ): 8.67 (d, J = 7.5 Hz, 2H), 8.56 (d, J = 8.2 Hz, 2H), 8.31 (s, 2H), 8.12 (t, J = 8.0 Hz, 2H), 7.51 (t, J = 4.2 Hz, 4H), 7.27 (s, 2H), 7.22 (d, J = 3.3 Hz, 2H), 7.06 (d, J = 3.2 Hz, 2H), 2.98 (d, J = 6.5 Hz, 4H), 1.85–1.72 (m, 2H), 1.58–1.22 (m, 20H), 1.02 (t, J = 7.4 Hz, 6H), 0.95 (dt, J = 7.2, 3.8 Hz, 6H). ^{13}C NMR (100 MHz, $CDCl_3$, δ): 146.50, 142.28, 136.46, 132.88, 131.80, 130.36, 129.76, 129.08, 128.47, 127.73, 127.41, 126.11, 125.53, 123.59, 123.22, 121.99, 41.68, 34.46, 32.60, 29.01, 25.91, 23.11, 14.24, 11.11.

4,10-Bis(2-thienyl)-6,12-bis(5-octyl-2-thienyl) anthanthrene (AANT-T-Sn). In a three-neck round-bottom flask, to a solution of **6** (249 mg, 0.3 mmol) in anhydrous THF (30 mL) was added a solution of *n*-BuLi in hexane (0.39 mL, 1.6 M) dropwise under nitrogen atmosphere at −78 °C. The mixture was stirred at −78 °C for 2 h, and the Bu_3SnCl (205 mg, 0.63 mmol) was added, and then warmed up to room temperature (RT) and stirred for 12 h. The mixture solution was quenched with H_2O, and exacted with chloroform (CF) (25 mL × 3). The organic extracts were washed with brine and dried over anhydrous $MgSO_4$. After removal of the solvents under the reduced pressure, the **AANT-T-Sn** (413 mg, 98.0%) was obtained as a orange solid, and used in the next step without any further purification. ^{1}H NMR (400 MHz, $CDCl_3$, δ): 8.83 (d, J = 7.9 Hz, 2H), 8.67–8.60 (m, 4H), 8.17 (d, J = 6.8 Hz, 2H), 7.68 (s, 2H), 7.55 (s, 2H), 7.40 (s, 2H), 4.29 (d, J = 4.9 Hz, 4H), 2.13 (s, 2H), 1.94–1.67 (m, 14H), 1.49–0.84 (m, 80H), 0.64–0.35 (m, 18H). Anal. calcd for: $C_{60}H_{68}S_4Sn_2$: C, 62.40; H, 5.94; S, 11.10. Found: C, 62.33; H, 5.98; S, 11.02.

AAN-DPP$_2$. In a three-neck round-bottom flask, under a nitrogen atmosphere, compounds **DPP-Bpi** (104 mg, 0.16 mmol) and **AAN** (55 mg, 0.08 mmol) were dissolved in 30 mL dry toluene, 2 M K_2CO_3 (0.8 mmol), Aliquat 336 (0.5 mL), then, $Pd(PPh_3)_4$ (5.5 mg, 0.0048 mmol) was added into the reaction mixture, and the reaction mixture was stirred vigorously for 12 h at 110 °C. The mixture was poured into H_2O and extracted with

DCM (25 mL × 3) and then dried over anhydrous $MgSO_4$. Then the organic solvent was evaporated under vacuum. The residue was purified by column chromatography (silica gel; eluent: PE : DCM = 1 : 1) to provide a purple solid **AAN-DPP$_2$** (88 mg, yield: 80%). ^{1}H NMR (400 MHz, $CDCl_3$, δ): 9.26 (s, 2H), 8.96 (s, 2H), 8.88 (s,2H), 8.67 (s, 4H), 8.21 (s, 2H), 7.74 (s, 2H), 7.66 (s, 2H), 7.29 (s, 2H), 4.31 (s, 4H), 4.14 (s, 8H), 2.12 (d, J = 32.1 Hz, 4H), 1.86 (d, J = 48.2 Hz, 10H), 1.71–1.64 (m, 2H), 1.26 (t, J = 55.5 Hz, 52H), 0.92 (s, 30H). ^{13}C NMR (100 MHz, $CDCl_3$, δ): 161.86, 150.59, 147.85, 140.41, 140.31–140.11, 136.56, 135.55–135.35, 130.56, 130.03, 128.46, 126.19, 124.82, 121.58–121.38, 46.17, 41.24, 39.29–39.10, 30.59, 30.26, 29.75, 29.37–29.17, 28.42, 24.06, 23.60, 23.15, 14.17, 11.53, 10.56. MALDI-MS (m/z) of $C_{98}H_{120}N_4O_6S_4$ for [M$^+$]: calcd 1577.81; found, 1578.029. Anal. calcd for: $C_{98}H_{120}N_4O_6S_4$: C, 74.58; H, 7.66; N, 3.55; S, 8.13. Found: C, 74.39; H, 7.42; N, 3.67; S, 8.04.

AAN(T-DPP)$_2$. In a three-neck round-bottom flask, under a nitrogen atmosphere, compounds **DPP-Br** (72 mg, 0.12 mmol) and **AAN-T-Sn** (61 mg, 0.06 mmol) were dissolved in 30 mL dry toluene, then, $Pd(PPh_3)_4$ (4.2 mg, 0.0036 mmol) was added into the reaction mixture, and the reaction mixture was stirred vigorously for 12 h at 110 °C. The mixture was poured into H_2O and extracted with DCM (25 mL × 3) and then dried over anhydrous $MgSO_4$. Then the organic solvent was evaporated under vacuum. The residue was purified by column chromatography (silica gel; eluent: PE : DCM = 1 : 1) to provide a deep purple solid **AAN(T-DPP)$_2$** (94 mg, yield: 90%). ^{1}H NMR (400 MHz, $CDCl_3$, δ): 8.95 (d, J = 3.6 Hz, 2H), 8.83 (d, J = 2.9 Hz, 2H), 8.70–8.44 (m, 6H), 8.01 (t, J = 7.2 Hz, 2H), 7.58 (d, J = 4.6 Hz, 2H), 7.49 (s, 4H), 7.37 (d, J = 3.6 Hz, 2H), 7.19 (s, 2H), 4.25 (d, J = 4.2 Hz, 4H), 4.04 (s, 8H), 2.11 (d, J = 5.6 Hz, 2H), 1.96 (d, J = 6.3 Hz, 4H), 1.80 (dd, J = 46.3, 6.7 Hz, 8H), 1.52–1.16 (m, 52H), 1.08–0.69 (m, 36H). ^{13}C NMR (100 MHz, $CDCl_3$, δ): 161.39, 142.83, 139.83, 136.14, 135.37–135.17, 130.33, 129.89, 128.34, 125.57, 124.70, 124.27, 119.08, 45.89, 41.34, 39.16, 30.77, 30.33, 29.56–29.36, 28.58, 24.08, 23.40, 23.19, 14.25, 11.77, 10.64. MALDI-MS (m/z) of $C_{106}H_{124}N_4O_6S_6$ for [M$^+$]: calcd 1741.79; found, 1741.91. Calcd for: $C_{106}H_{124}N_4O_6S_6$: C, 73.06; H, 7.17; N, 3.22; S, 11.04. Found: C, 72.97; H, 7.08; N, 3.15; S, 10.93.

AANT(T-DPP)$_2$. In a three-neck round-bottom flask, compounds **DPP-Br** (96 mg, 0.16 mmol) and **AANT-T-Sn** (92 mg, 0.08 mmol) were dissolved in 30 mL dry toluene, $Pd(PPh_3)_4$ (5.5 mg, 0.0048 mmol) was added into the reaction mixture. The reaction mixture was stirred vigorously for 12 h at 110 °C under nitrogen atmosphere. The resulting mixture was poured into H_2O and extracted with DCM (25 mL × 3) and then dried over anhydrous $MgSO_4$. The organic solvent was evaporated under vacuum. The residue was purified by column chromatography (silica gel; eluent: PE : DCM = 1 : 1) to provide a deep blue solid **AANT(T-DPP)$_2$** (135 mg, yield: 90%). ^{1}H NMR (400 MHz, $CDCl_3$, δ): 8.99 (d, J = 4.1 Hz, 2H), 8.89 (d, J = 3.8 Hz, 2H), 8.70 (d, J = 7.6 Hz, 2H), 8.57 (d, J = 8.2 Hz, 2H), 8.32 (s, 2H), 8.13 (t, J = 8.0 Hz, 2H), 7.63 (d, J = 5.0 Hz, 4H), 7.45 (d, J = 3.5 Hz, 2H), 7.43 (d, J = 3.6 Hz, 2H), 7.39 (d, J = 4.1 Hz, 2H), 7.28 (d, J = 4.3 Hz, 2H), 7.22 (d, J = 3.3 Hz, 2H), 7.06 (d, J = 3.2 Hz, 2H), 4.06 (d, J = 6.8 Hz, 8H), 2.97 (d, J = 6.8 Hz, 4H), 1.92 (d, J = 29.7 Hz, 4H), 1.76 (dd, J = 12.6, 6.4 Hz, 2H), 1.41–1.22 (m, 48H), 0.94 (ddd, J = 13.0, 12.3, 6.0 Hz, 36H). ^{13}C NMR (100 MHz, $CDCl_3$, δ): 161.69, 146.65, 143.34, 142.67, 139.91, 136.89, 136.27, 135.18, 132.17, 131.80, 130.40, 130.04–129.50, 129.42, 128.95, 128.48, 128.12, 126.27, 125.51, 124.79, 123.40, 121.97, 108.19, 45.97, 41.68, 39.21, 34.43, 32.68, 30.32, 29.72, 29.00, 28.49, 25.97, 23.67, 23.11, 14.45–13.85, 11.13, 10.58. MALDI-MS (m/z) of $C_{114}H_{128}N_4O_4S_8$ for [M$^+$]: calcd 1873.77; found, 1873.583. Calcd for: $C_{114}H_{128}N_4O_4S_8$: C, 73.04; H, 6.88; N, 2.99; S, 13.68. Found: C, 73.01; H, 6.94; N, 3.04; S, 13.56.

3. Results and discussion

3.1. Thermal property

The thermal properties of **AAN-DPP$_2$**, **AAN(T-DPP)$_2$** and **AANT(T-DPP)$_2$** were characterized by thermogravimetric analyses (TGA) at a heating rate of 10 °C min^{-1} under the nitrogen atmosphere. The TGA curves are depicted in Fig. 1, and their thermal parameters are summarized in Table 1. The thermal decomposition temperatures (T_d) of 331 °C for **AAN-DPP$_2$**, 331 °C for **AANT(T-DPP)$_2$** and 421 °C for **AANT(T-DPP)$_2$** are exhibited at a 5% weight loss. It indicates that all the three small molecules have high thermal stability. Fig. 2 depicts the differential scanning calorimetry (DSC) plots of **AAN-DPP$_2$**, **AAN(T-DPP)$_2$** and **AANT(T-DPP)$_2$** in solid state. The typical endothermal peaks at 218, 222 and 203 °C were observed for **AAN-DPP$_2$**, **AAN(T-DPP)$_2$** and **AANT(T-DPP)$_2$** during the heating process, which correspond to melting temperatures (T_m), respectively. However, only **AAN-DPP$_2$** and **AAN(T-DPP)$_2$** displayed an exothermal peak at 201 °C and 209 °C during the cooling process. It indicates that **AAN-DPP$_2$** and **AAN(T-DPP)$_2$** has the higher melting temperature and better crystallinity than **AANT(T-DPP)$_2$**, further promoting π–π stacking and charge transport.[40] Especially, as shown in Fig. 2, **AAN(T-DPP)$_2$** exhibits the sharpest exothermal peak of the three molecules, which implies that **AAN(T-DPP)$_2$** is likely to obtain the best charge transport mobility.[9]

3.2. Optical properties

To further investigate the relationship between the molecular structure and the corresponding photophysical property, the UV-Vis absorption spectra of three SMs in dilute chloroform solution and in neat films are displayed respectively in Fig. 2, and the related data are listed in Table 2. As shown in Fig. 2a, the absorption bands of 300–480 nm and 500–650 nm are ascribed to the π–π* transition of conjugated backbone and intramolecular charge transfer (ICT), respectively. Compared to the absorption profiles of **AAN-DPP$_2$**, **AAN(T-DPP)$_2$** and **AANT(T-DPP)$_2$** exhibit a stronger absorption in the short-wavelength, which attribute to the inserting of the thiophene unit to enhance the π–π* transition. Meanwhile, in the absorption of long-wavelength, **AAN(T-DPP)$_2$** and **AANT(T-DPP)$_2$** show a distinct red-shift in comparison with that of **AAN-DPP$_2$**, which is assigned to the longer conjugated backbone and stronger D/A intramolecular charge transfer. As presented in Fig. S20,† the maximum absorption coefficient (ε) values of the **AAN-DPP$_2$**, **AAN(T-DPP)$_2$** and **AANT(T-DPP)$_2$** are to be 4.61 × 10^4 cm^{-1} M^{-1},

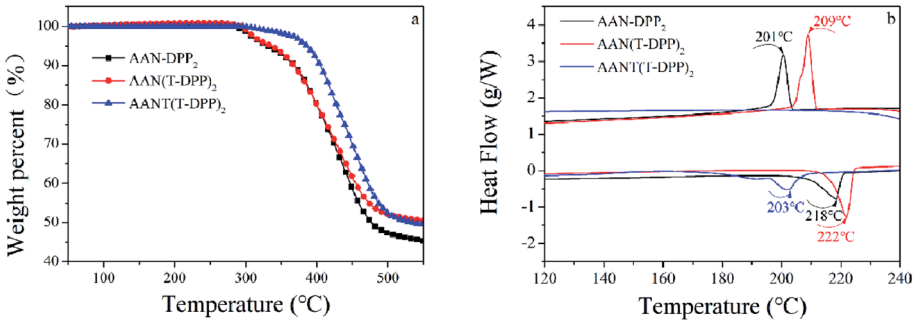

Fig. 1 (a) TGA and (b) DSC thermograms of SMs under nitrogen atmosphere at a scan rate of 10 °C min^{-1}.

Table 1 TGA and DSC patterns of SMs

SMs	T_d (°C)	T_m (°C)	T_c (°C)
AAN-DPP$_2$	331	218	201
AAN(T-DPP)$_2$	331	222	209
AANT(T-DPP)$_2$	388	203	—

5.03×10^4 cm^{-1} M^{-1}, 5.35×10^4 cm^{-1} M^{-1} at low-lying energy area, respectively. The higher ε value is expected to absorb more solar photons, which is conducive to obtaining higher J_{sc} values in its OSCs with the same thickness of active layer.

Compared to the absorption profiles in solutions, due to the additional intermolecular π–π stacking in this state, the broadened and red-shifted absorption profiles for these SMs in thin films are observed in Fig. 2b, and the detailed absorption parameters are summarized in Table 1. As results, the **AAN-DPP$_2$**, **AAN(T-DPP)$_2$** and **AANT(T-DPP)$_2$** exhibit a 38, 62, and 89 nm red-shifted absorption profiles than that in solutions, respectively, which implies that **AAN(T-DPP)$_2$** and **AANT(T-DPP)$_2$** has stronger intermolecular interactions in thin solid film. Furthermore, the obvious additional peaks at 592, 624, and 624 nm are obtained in **AAN-DPP$_2$**, **AAN(T-DPP)$_2$** and **AANT(T-DPP)$_2$**, respectively, which result from the strong intermolecular packing potentials in a solid state, respectively. Furthermore, based on the onset of film absorption, the optical band gaps (E_g^{opt}) are determined to be 1.90 eV for **AAN-DPP$_2$**, 1.76 eV for **AAN(T-DPP)$_2$** and 1.70 eV for **AANT(T-DPP)$_2$**, respectively. The lower band gaps of **AAN(T-DPP)$_2$** and **AANT(T-DPP)$_2$** are observed. Clearly, the unit of thiophene π-bridge here plays a positive role in decreasing optical band gaps. It illustrates that obtaining a longer effective π-conjugated system by introducing thiophene π-bridge is an effective way to decreasing the optical band gaps of their resulting SMs and broaden the absorption in the long-wavelength region, which result in the enhancement of J_{sc}.

3.3. Electrochemical properties

Electrochemical properties of **AAN-DPP$_2$**, **AAN(T-DPP)$_2$** and **AANT(T-DPP)$_2$** were investigated by cyclic voltammetry (CV) using a standard three electrodes electrochemical cell. As shown in Fig. 3, the onset oxidation/reduction potentials of **AAN-DPP$_2$**, **AAN(T-DPP)$_2$** and **AANT(T-DPP)$_2$** are 0.93/−0.89, 0.90/−0.82, and 0.92/−0.74 V, respectively. HOMO levels of **AAN-DPP$_2$**, **AAN(T-DPP)$_2$** and **AANT(T-DPP)$_2$** were determined by the equation $E_{HOMO} = -(E_{ox} + 4.31)$, to be −5.24, −5.21, and −5.23 eV, respectively. LUMO levels of **AAN-DPP$_2$**, **AAN(T-DPP)$_2$** and **AANT(T-DPP)$_2$** were therefore calculated from the equation $E_{LUMO} = -(E_{red} + 4.31)$, to be −3.42, −3.49, and −3.57 eV, respectively. The data are summarized in Table 2. The results indicated that the introduction of thiophene units would only slightly higher the HOMO energy level of small molecules. Their low-lying HOMO level is favorable for achieving SMSCs with higher V_{oc}. The changing of thiophene substituent group on the donor core unit has a subtle influence on their electrochemical properties.

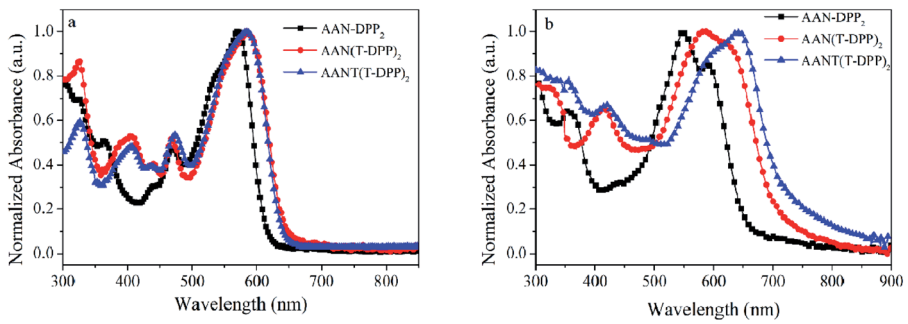

Fig. 2 Normalized UV-vis absorption spectra of SMs in (a) dilute $CHCl_3$ and (b) in their neat films at RT, respectively.

Table 2 Optical and electrochemical properties of SMs[a]

SMs	λ_{max} (nm) Solution	Film	λ_{onset} (nm)	E_g^{opt} [b] (eV)	E_{ox}^{on} (V)	E_{red}^{on} (V)	E_{HOMO} [c] (eV)	E_{LUMO} [c] (eV)	E_g^{ele} (eV)
SM1	324,569	353,549	650	1.90	0.93	−0.89	−5.24	−3.42	1.82
SM2	324, 407,582	413,586	703	1.76	0.90	−0.82	−5.21	−3.49	1.72
SM3	326,409,590	420,642	729	1.70	0.92	−0.74	−5.23	−3.57	1.66

[a] SM1, SM2 and SM3 represent for **AAN-DPP$_2$**, **AAN(T-DPP)$_2$** and **AANT(T-DPP)$_2$**, respectively. [b] Calculated from the absorption band edge of the films, $E_g^{opt} = 1240/\lambda_{onset}$. [c] Calculated from empirical equation: $E_{HOMO} = -(E_{ox} + 4.31)$ eV and $E_{LUMO} = -(E_{red} + 4.31)$ eV; the formal potential of F_c/F_c^+ was 0.49 V *vs.* Ag/AgCl measured in this work.

3.4. Theoretical calculations

In order to gain a deeper understanding of the impact of selecting different acceptors on the geometrical conformations and energy levels of the SMs, the HOMO and LUMO distributions of these SMs were calculated by the density functional theory (DFT) (B3LYP; 6-31G*) method. Fig. 4a shows their optimized geometric structures, experimental energy levels and the electron-state-density distributions in the molecular orbital. The different coplanarity between the aromatic rings is observed. The dihedral angles between the **AAN** central core and the thiophene-bridge were calculated to be 50.277°, 48.122° and 46.290° for **AAN-DPP$_2$**, **AAN(T-DPP)$_2$** and **AANT(T-DPP)$_2$**, respectively. Moreover, the dihedral angles between the thiophene-bridge and the aromatic ring of three SMs were calculated to be 18.545°, 12.538° and 13.073° for **AAN-DPP$_2$**, **AAN(T-DPP)$_2$** and **AANT(T-DPP)$_2$**, respectively. Obviously, **AAN(T-DPP)$_2$** and **AANT(T-DPP)$_2$** have a better molecular planarity than that of **AAN-DPP$_2$**, especially, the planarity of **AAN(T-DPP)$_2$** is outstanding in three SMs. The better molecular planarity for **AAN(T-DPP)$_2$** and **AANT(T-DPP)$_2$**, which can promote intermolecular π–π stacking, further good for increasing FF value of their devices. As is shown in Fig. 4b, the electron densities is delocalized over the whole molecular backbone both in the HOMO wave function and the LUMO wave function for **AAN-DPP$_2$**, **AAN(T-DPP)$_2$** and **AANT(T-DPP)$_2$**. It is different that the HOMO is mainly distributed on the moieties of electron-rich **AAN** and the LUMO is mainly distributed on the moieties of electron-deficient DPP, owing to a strong ICT effect.[27–34] The calculated HOMO energy level of **AAN-DPP$_2$** is 0.21 eV lower than that of **AAN(T-DPP)$_2$** and **AANT(T-DPP)$_2$**, respectively, which is in accordance with the tendency of the CV data.

3.5. Hole mobility

The hole mobility of the active layer play an important role in the resulting photovoltaic performance of SMSCs, especially on FF.[41] We measured the hole-only mobilities (μ_h) of **AAN-DPP$_2$**, **AAN(T-DPP)$_2$** and **AANT(T-DPP)$_2$** blended with $PC_{71}BM$, respectively, at optimized condition by the space charge limited current (SCLC) method with a typical device structure of ITO/PEDOT:PSS/SMs:$PC_{71}BM$/Au. The SCLC could be estimated using the Mott–Gurney equation: $J = (9/8)\varepsilon_0\varepsilon_r\mu_h(V^2/L^3)$,[42,43] where, J is current density, ε_r is dielectric constant of polymer (3.0), ε_0 is free-space permittivity (8.85×10^{-12} F m^{-1}), $V = V_{appl} - V_{bi}$, V is the effective voltage, V_{appl} is applied voltage, and V_{bi} is built-in voltage that results from the work function difference between the anode and cathode. As shown in Fig. 5, the μ_h of **AAN-DPP$_2$**, **AAN(T-DPP)$_2$** and **AANT(T-DPP)$_2$** were calculated to be 1.23×10^{-5} cm^2 V^{-1} s^{-1}, 7.61×10^{-5} cm^2 V^{-1} s^{-1}, and 5.07×10^{-5} cm^2 V^{-1} s^{-1}. Obviously, the μ_h of **AAN(T-DPP)$_2$** shows a certain increase, which implies that the relatively higher FF could be obtained in the SMSCs.[44–48]

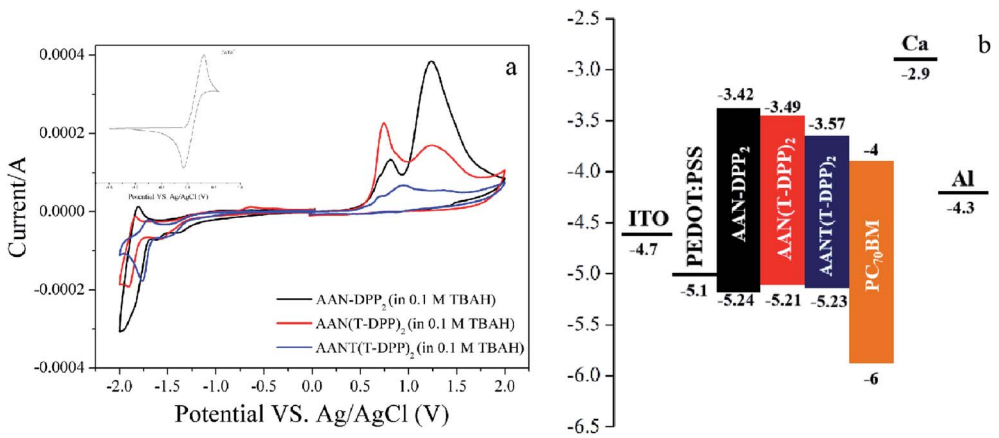

Fig. 3 (a) CV curves of SMs at a scan rate of 50 mV s^{-1} and (b) schematic energy diagram of the materials used in the SM-OSCs.

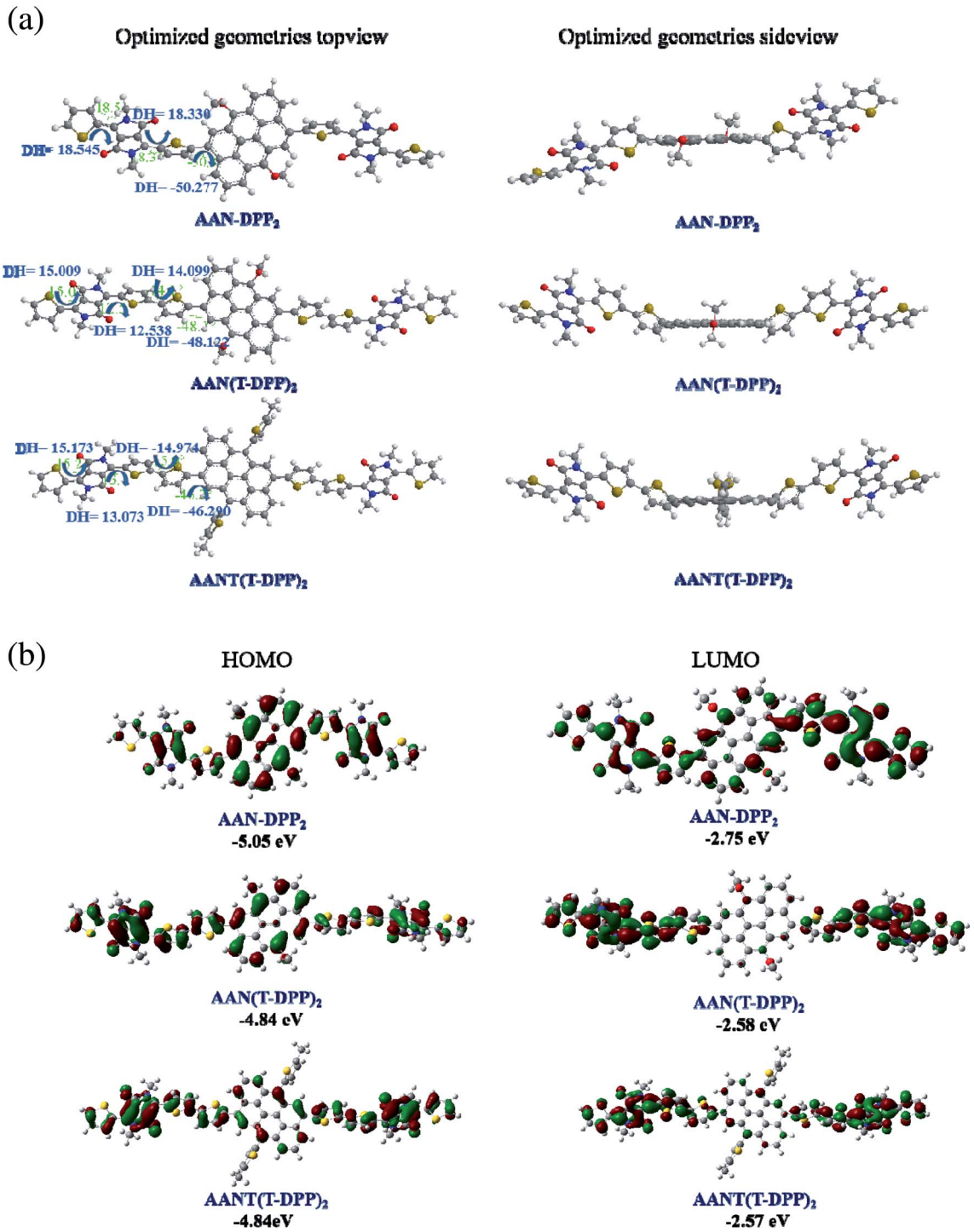

Fig. 4 (a) Optimized molecular geometries and (b) molecular frontier orbitals of HOMO and LUMO for SMs obtained by Gaussian 09 at the B3LYP/6-31G(d) level.

3.6. Photovoltaic properties

To investigate the photovoltaic properties of **AAN-DPP$_2$**, **AAN(T-DPP)$_2$** and **AANT(T-DPP)$_2$**, respectively, the BHJ SMSCs were also fabricated with a typical device structure of ITO/PEDOT:PSS/SMs/Ca/Al. The active layer of SMs/$PC_{71}BM$ was obtained from a $CHCl_3$ solution at a concentration of 12 mg mL^{-1} for **AAN-DPP$_2$**, **AAN(T-DPP)$_2$** with a spin-coating rate of 5000 rpm and a thickness of 90 nm; at the same time, result from the relatively poor solubility in the three small molecules, 10 mg mL^{-1} for **AANT(T-DPP)$_2$** with a spin-coating rate of 3000 rpm and a thickness of 80 nm was obtained for the active layer of **AANT(T-DPP)$_2$**/$PC_{71}BM$. As demonstrated, the photovoltaic performances of SMSCs are strongly affected by the processing

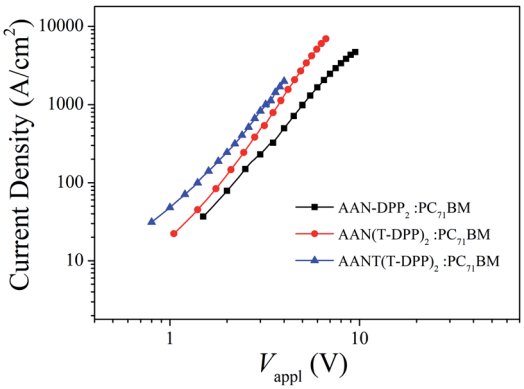

Fig. 5 *J*–*V* curve of the hole-only SMs: $PC_{71}BM$-based devices under the optimized processing conditions.

parameters,[34] including the D/A ratio (w/w), spin-coating rate and annealing temperature, these optimized parameters were obtained and showed at Fig. S21–S28 (see ESI†), respectively. The corresponding photovoltaic data are summarized in Tables S1–S8 (see ESI†), respectively. As a result, the SMs/$PC_{71}BM$-based SMSCs have an optimized D/A ratio of 1 : 4 for **AAN-DPP$_2$**, **AANT(T-DPP)$_2$** and 1 : 3 for **AAN(T-DPP)$_2$**, annealing temperature of 70 °C, without any additive, respectively. As shown in Fig. 6, the SMSCs exhibited the typical *J*–*V* characteristics under optimized conditions, and the device parameters, such as J_{sc}, V_{oc}, FF and PCE were summarized in Table 3, and the detailed PCE distribution of all devices under optimized conditions were displayed in Fig. S29 (see ESI†). Encouragingly, the SMs/$PC_{71}BM$-based SMSCs showed outstanding photovoltaic performance of high open-circuit voltage, in which the maximum PCE of **AAN(T-DPP)$_2$** is 2.33% with a V_{oc} of 0.86 V, a J_{sc} of 6.82 mA cm^{-2}, and an FF of 39.8%. And the maximum PCE of **AAN-DPP$_2$** is 1.92% with an FF of 34.25%, a J_{sc} of 6.12 mA cm^{-2}, and a V_{oc} of up to 0.92 V. Furthermore, the maximum PCE of **AANT(T-DPP)$_2$** is 2.03% with an FF of 36.12%, a J_{sc} of 6.25 mA cm^{-2}, and a V_{oc} of up to 0.90 V. To our knowledge, the recorded maximum V_{oc} values here is one of the highest than that of the previous diketopyrrolopyrrole (DPP) based on small molecular derivatives in BHJ OSCs.[9,34,44] Notably, **AANT(T-DPP)2**-based device obtained a relatively lower J_{sc} of 6.25 mA cm^{-2} compare with that of **AAN(T-DPP)$_2$**, which may be result from the relatively poorer solubility and thinner thickness of active layer for **AANT(T-DPP)$_2$**. Though the higher ε value is obtained for **AANT(T-DPP)$_2$**, which was expected to get a higher J_{sc} value. The results illustrate that substitute the suitable side modified groups onto the backbone to adjust the solubility of the whole molecule is important for SMSCs to get higher photovoltaic efficiency. Furthermore, the results also indicate that molecular modification by introducing two thiophene units to the huge polycyclic aromatic core of anthanthrene (**AAN**) will be a promising strategy to decrease the torsion angle of the whole molecule and increase the FF of the low bandgap conjugated small molecules, further enhancing the photovoltaic performance of SMSCs. As expection, compared to the similar non-thiophene modified donor core based **AAN-DPP$_2$**, **AAN(T-DPP)$_2$** and **AANT(T-DPP)$_2$** shows an increased J_{sc}, which is match well with the results of UV-vis absorption test. Although both of the molecules possess relatively higher HOMO levels, which attributable to the slightly lower open-circuit voltage of **AAN(T-DPP)$_2$** and **AANT(T-DPP)$_2$**.[33,34]

To understand the reason of **AAN-DPP$_2$**, **AAN(T-DPP)$_2$** and **AANT(T-DPP)$_2$**/$PC_{71}BM$ based devices displayed higher PCE values, the external quantum efficiency (EQE) curves of devices under the optimized conditions were also measured. As depicted in Fig. 6, the **AAN-DPP$_2$**, **AAN(T-DPP)$_2$** and **AANT(T-DPP)$_2$**/$PC_{71}BM$ based device show very efficient photo-response in a broad range from 300 to 750 nm, corresponding to high EQE over 30% in a broad range from 348 to 600 nm. With the maximum EQE of 40.32% at 470 nm for **AAN-DPP$_2$**, the maximum EQE of 45.47% at 500 nm for **AAN(T-DPP)$_2$**, and the maximum EQE of 42.34% at 466 nm for **AANT(T-DPP)$_2$**, is observed for the device. Obviously, high EQE value is responsible for high J_{sc} of **AAN-DPP$_2$**, **AAN(T-DPP)$_2$** and **AANT(T-DPP)$_2$** based SMSCs. According to the EQE curve and the solar irradiation spectrum, the integral J_{sc} value is 5.91 mA cm^{-2}, 6.39 mA cm^{-2} and 6.06 mA cm^{-2} for **AAN-DPP$_2$**, **AAN(T-DPP)$_2$**, and **AANT(T-DPP)$_2$** based SMSCs, which is coincident with the measured J_{sc} value around a 5% error. It indicates that our photovoltaic measurement is accurate and reliable.

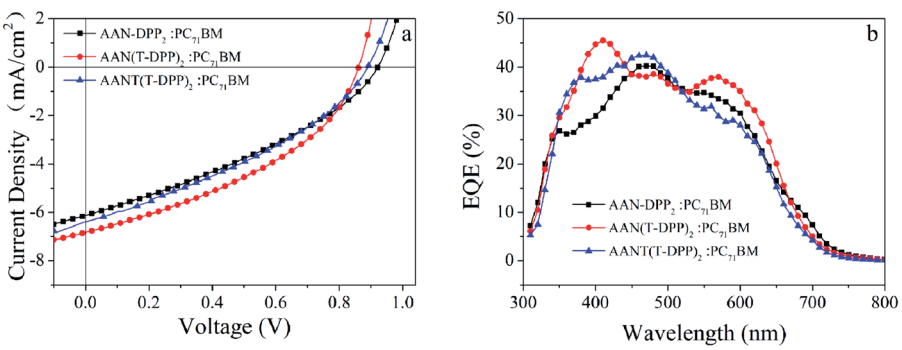

Fig. 6 (a) *J*–*V* curves and (b) EQE spectra of the SMs/$PC_{71}BM$ cells at the optimized SMs/$PC_{71}BM$ devices under AM.1.5 G illumination (100 mW cm^{-2}).

Table 3 Photovoltaic and hole mobilities data of the optimized devices based on SMs[a]

Active layer	D/A [w/w]	V_{oc} (V)	J_{sc} (mA cm^{-2})	FF (%)	$PCE_{max/ave}$ (%)	μ_h (cm^2 V^{-1} s^{-1})
SM1:$PC_{71}BM$[b]	1:4	0.92	6.12	34.25	1.92(1.75)[d]	1.23×10^{-5}
SM2:$PC_{71}BM$[b]	1:3	0.86	6.82	39.80	2.33(2.14)[d]	7.61×10^{-5}
SM3:$PC_{71}BM$[c]	1:4	0.90	6.25	36.12	2.03(1.87)[d]	5.07×10^{-5}

[a] SM1, SM2 and SM3 represent for **AAN-DPP$_2$**, **AAN(T-DPP)$_2$** and **AANT(T-DPP)$_2$**, respectively. [b] Blending with $PC_{71}BM$, spin-coating rate 5000 rpm, 12 mg mL^{-1} in solvent CF. [c] Spin-coating rate 3000 rpm, 10 mg mL^{-1} in solvent CF, CF = chloroform. [d] Average device performance obtained form 10 devices.

4. Conclusions

In conclusion, a series of A–D–A type small molecules were synthesized and investigated. These small molecules exhibited a broad absorption in the range of 300–750 nm, a low-lying HOMO energy level of −5.24 eV, a good carrier mobility of 5.05×10^{-4} cm^2 V^{-1} s^{-1}, and an outstanding V_{oc} of 0.92 V, which is among one of the highest V_{oc} value in the reported DPP-based OSCs. And a best PCE of 2.33% was obtained on **AAN(T-DPP)$_2$**-based OSCs, the results indicate that introducing thiophene π-bridges and suitable side modified groups onto the anthanthrene (**AAN**) donor core is a promising strategy to decrease the torsion angle of the whole molecule, and to increase the FF value of small molecules which with a bulky fused planar core, and for further enhancing the photovoltaic performance of SMSCs.

Conflicts of interest

There are no conflicts to declare.

Acknowledgements

Thanks to the financial supports from the Research Foundation for Advanced Talents of East China University of Technology (DHBK2019142), the School of Materials Science and Engineering, Jiangsu Engineering Laboratory of Light-Electricity-Heat Energy-Converting Materials and Applications (GDRGCS2020002).

References

1 J. Chen and Y. Cao, *Acc. Chem. Res.*, 2009, **42**, 1709–1718.
2 Y. J. Cheng, S. H. Yang and C. S. Hsu, *Chem. Rev.*, 2009, **109**, 5868–5923.
3 G. Li, R. Zhu and Y. Yang, *Nat. Photonics*, 2012, **6**, 153–161.
4 Y. Li, *Acc. Chem. Res.*, 2012, **45**, 723–733.
5 B. Fan, D. Zhang, M. Li, W. Zhong, Z. Zeng, L. Ying, F. Huang and Y. Cao, *Sci. China: Chem.*, 2019, **62**, 746–752.
6 X. P. Xu, K. Feng, Z. Z. Bi, W. Ma, G. J. Zhang and G. J. Peng, *Adv. Mater.*, 2019, **31**, 1901872.
7 Q. S. Liu, Y. F. Jiang, K. Jin, J. Q. Qin, J. G. Xu, W. T. Li, J. Xiong, J. F. Liu, Z. Xiao, K. Sun, S. F. Yang, X. T. Zhang and L. M. Ding, *Sci. Bull.*, 2020, **65**, 272–275.
8 L. X. Meng, Y. M. Zhang, X. J. Wan, C. X. Li, X. Zhang, Y. B. Wang, X. Ke, Z. Xiao, L. M. Ding, R. X. Xia, H. L. Yip, Y. Cao and Y. S. Chen, *Science*, 2018, **361**, 1094–1098.
9 J. L. Wang, H. J. Zhang, S. Liu, K. K. Liu, F. Liu, H. B. Wu and Y. Cao, *Sol. RRL*, 2018, **2**, 1800108.
10 J. L. Wang, K. K. Liu, J. Yan, Z. Wu, F. Liu, F. Xiao, Z. F. Chang, H. B. Wu, Y. Cao and T. P. Russell, *J. Am. Chem. Soc.*, 2016, **138**, 7687–7697.
11 J. H. Wan, X. P. Xu, G. J. Zhang, Y. Li, K. Feng and Q. Peng, *Energy Environ.*, 2017, **10**, 1739–1745.
12 M. Li, Z. B. Qiu, G. J. Zhang, Y. Liu, L. Xiong, D. Bai, M. B. Zhu, Q. Peng and W. G. Zhu, *J. Mater. Chem. A*, 2018, **6**, 12493–12505.
13 W. Ni, X. J. Wan, M. M. Li, Y. C. Wang and Y. S. Chen, *Chem. Commun.*, 2015, **51**, 4936–4950.
14 S. Qu and H. Tian, *Chem. Commun.*, 2012, **48**, 3039–3051.
15 S. Y. Liu, W. Q. Liu, J. Q. Xu, C. C. Fan, W. F. Fu, J. Ling, J. Y. Wu, M. M. Shi, A. K. Jen and H. Z. Chen, *ACS Appl. Mater. Interfaces*, 2014, **6**, 6765–6775.
16 W. S. Yoon, S. K. Park, I. Cho, J. A. Oh, J. H. Kim and S. Y. Park, *Adv. Funct. Mater.*, 2013, **23**, 3519–3524.
17 A. Tang, C. L. Zhan, J. N. Yao and E. J. Zhou, *Adv. Mater.*, 2017, **29**, 1600013.
18 H. Choi, S. J. Ko, T. Kim, P. O. Morin, B. Walker, B. H. Lee, M. Leclerc, J. Y. Kim and A. J. Heeger, *Adv. Mater.*, 2015, **27**, 3318–3324.
19 W. Li, K. H. Hendriks, M. M. Wienk and R. A. Janssen, *Acc. Chem. Res.*, 2016, **49**, 78–85.
20 R. S. Ashraf, I. Meager, M. Nikolka, M. Kirkus, M. Planells, B. C. Schroeder, S. Holliday, M. Hurhangee, C. B. Nielsen, H. Sirringhaus and I. McCulloch, *J. Am. Chem. Soc.*, 2015, **137**, 1314–1321.
21 M. Desroches and J. F. Morin, *Org. Lett.*, 2018, **20**, 2797–2801.
22 D. J. Stewart, J. M. Shi, T. R. Naranjo, T. A. Grusenmeyer, J. M. Artz, C. L. McCleese, R. M. O'Donnell, T. M. Cooper, W. M. Shensky and J. E. Haley, *Phys. Chem. Chem. Phys.*, 2018, **20**, 28412.
23 T. Matsuno, S. Kamata, S. Hitosugi and H. Isobe, *Chem. Sci.*, 2013, **4**, 3179–3183.
24 J. B. Giguere and J. F. Morin, *J. Org. Chem.*, 2013, **78**, 12769.
25 J. F. Gigu`ere, N. S. Sariciftcib and J. F. Morin, *J. Mater. Chem. C*, 2015, **3**, 601–606.
26 M. S. Chen, J. R. Niskala, D. A. Unruh, C. K. Chu, O. P. Lee and J. M. Frechet, *J. Chem. Mater.*, 2013, **25**, 4088–4096.

27 T. Wang, Y. H. Chen, X. C. Bao, Z. K. Du, J. Guo, N. Wang, M. L. Sun and R. Q. Yang, *Dyes Pigm.*, 2013, **98**, 11–16.
28 H. Sun, X. Song, J. Xie, P. Sun, P. Y. Gu, C. M. Liu, F. Chen, Q. C. Zhang, Z. K. Chen and W. Huang, *ACS Appl. Mater. Interfaces*, 2017, **9**, 29924–29931.
29 W. Q. Chen and Q. C. Zhang, *J. Mater. Chem. C*, 2017, **5**, 1275–1302.
30 W. Q. Chen, X. Yang, G. k. Long, X. J. Wan, Y. S. Chen and Q. C. Zhang, *J. Mater. Chem. C*, 2015, **3**, 4698–4705.
31 J. L. Wang, Q. R. Yin, J. S. Miao, Z. Wu, Z. F. Chang, Y. Cao, R. B. Zhang, J. Y. Wang, H. B. Wu and Y. Cao, *Adv. Funct. Mater.*, 2015, **25**, 3514–3523.
32 S. W. Shi, P. Jiang, S. Chen, Y. P. Sun, X. C. Wang, K. Wang, S. L. Shen, X. Y. Li, Y. F. Li and H. Q. Wang, *Macromolecules*, 2012, **45**, 7806–7814.
33 Z. F. Ma, D. F. Dang, Z. Tang, D. Gedefaw, J. Bergqvist, W. G. Zhu, W. Mammo, M. R. Andersson, O. Inganäs, F. L. Zhang and E. G. Wang, *Adv. Energy Mater.*, 2014, **4**, 1301455.
34 M. Li, G. J. Zhang, L. Xiong, M. B. Zhu, Y. Pei, Q. Peng and Y. Liu, *Dyes Pigm.*, 2018, **158**, 402–411.
35 L. Ye, S. Q. Zhang, L. J. Huo, M. J. Zhang and J. H. Hou, *Acc. Chem. Res.*, 2014, **47**, 1595–1603.
36 M. Wang, X. W. Hu, P. Liu, W. Li, X. Gong and F. Huang, *J. Am. Chem. Soc.*, 2011, **133**, 9638–9641.
37 J. B. Giguere, Q. Verolet and J. F. Morin, *Chem.–Eur. J.*, 2013, **19**, 372–381.
38 Y. Z. Lin, L. C. Ma, Y. F. Li, Y. Q. Liu, D. B. Zhu and X. W. Zhan, *Adv. Energy Mater.*, 2013, **3**, 1166–1170.
39 Y. Zhao, X. Zhou, K. L. Wu, H. Wang, S. W. Qu, F. He and C. L. Yang, *Dyes Pigm.*, 2016, **130**, 282–290.
40 J. Huang, C. Zhan, X. Zhang, Y. Zhao, Z. Lu, H. Jia and J. Yao, *ACS Appl. Mater. Interfaces*, 2013, **5**, 2033–2039.
41 J. H. Kim, H. S. Shim, H. Lee, M. S. Choi, J. J. Kim and Y. S. Seo, *J. Phys. Chem. C*, 2014, **118**, 11559–11565.
42 P. W. M. Blom, V. D. L. Mihailetchi, J. A. Koster and D. E. Markov, *Adv. Mater.*, 2007, **19**, 1551–1566.
43 A. M. Goodman and A. Rose, *J. Appl. Phys.*, 1971, **42**, 2823–2830.
44 M. Li, S. C. Wang, C. J. Bao, Z. J. Liu, D. Bai, Z. Yang, W. G. Zhu, Q. Peng and Y. Liu, *J. Mater. Chem. C*, 2019, **7**, 12217–12230.
45 P. Zhou, D. F. Dang, Q. Wang, X. W. Duan, M. J. Xiao, Q. Tao, H. Tan, R. Q. Yang and W. G. Zhu, *J. Mater. Chem. A*, 2015, **3**, 13568–13576.
46 M. Li, Z. J. Li, Z. Yang, Z. J. Liu, K. Zhang, L. Yang, Q. Peng, W. G. Zhu and Y. Liu, *Dyes Pigm.*, 2019, **170**, 107595.
47 Z. J. Li, R. P. Liang, J. W. Wang, B. Na and H. S. Liu, *J. Phys. Chem. C*, 2019, **123**, 28021–28026.
48 M. D. Perez, C. Borek, S. R. Forrest and M. E. Thompson, *J. Am. Chem. Soc.*, 2009, **131**, 9281–9286.